

RENO: Real-Time Neural Compression for 3D LiDAR Point Clouds

Kang You¹, Tong Chen^{1*}, Dandan Ding², M. Salman Asif³, Zhan Ma¹

¹Nanjing University, ²Hangzhou Normal University, ³University of California Riverside
 youkang@smail.nju.edu.cn, chentong@nju.edu.cn, dandanding@hznu.edu.cn,
 sasif@ucr.edu, mazhan@nju.edu.cn

Abstract

Despite the substantial advancements demonstrated by learning-based neural models in the LiDAR Point Cloud Compression (LPCC) task, realizing real-time compression—an indispensable criterion for numerous industrial applications—remains a formidable challenge. This paper proposes RENO, the first real-time neural codec for 3D LiDAR point clouds, achieving superior performance with a lightweight model. RENO skips the octree construction and directly builds upon the multiscale sparse tensor representation. Instead of the multi-stage inferring, RENO devises sparse occupancy codes, which exploit cross-scale correlation and derive voxels’ occupancy in a one-shot manner, greatly saving processing time. Experimental results demonstrate that the proposed RENO achieves real-time coding speed, 10 fps at 14-bit depth on a desktop platform (e.g., one RTX 3090 GPU) for both encoding and decoding processes, while providing 12.25% and 48.34% bit-rate savings compared to G-PCCv23 and Draco, respectively, at a similar quality. RENO model size is merely 1MB, making it attractive for practical applications. The source code is available at <https://github.com/NJUVISION/RENO>.

1. Introduction

LiDAR point clouds serve as essential representations of 3D environments and are widely utilized in robotics [34, 45], autonomous driving [4, 14, 24], and 3D mapping [25, 49]. In time-critical applications, such as autonomous driving, the continuous influx of point cloud data necessitates advanced and real-time¹ LiDAR Point Cloud Compression (LPCC) techniques to effectively facilitate on-device storage [1], network transmission [21], and collaborative decision-making [6] within dynamic environments.

*Corresponding author.

¹Such a “real-time” criteria is defined by the frequency to collect LiDAR data, which is typically set to 10 Hz.

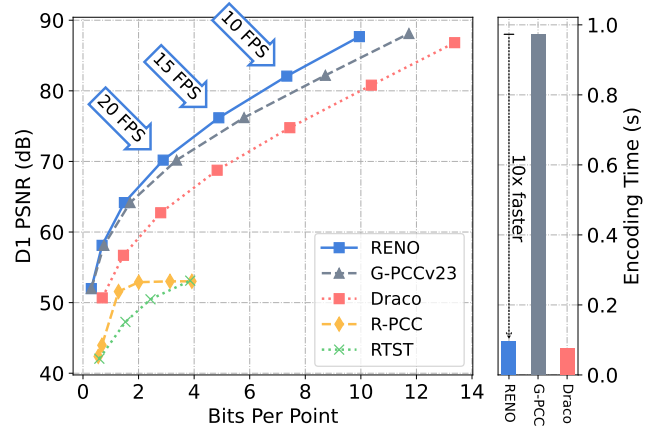


Figure 1. Left: Rate distortion performance comparison on the KITTI dataset. Right: Encoding time comparison for 14 bit (± 8 mm precision) LiDAR scan, where RENO operates $10 \times$ faster than the latest G-PCCv23 standard, achieving a runtime of 10 frames per second. Notably, the encoding time encompasses all durations including preprocessing, network inference, and arithmetic coding. Our decoding time is comparable to the encoding.

Conventional rules-based LPCC methods face significant challenges in balancing rate-distortion performance and low compression latency. For example, the Moving Picture Experts Group (MPEG) committee has introduced the G-PCC standard [19, 41], which is implemented in the TMC13 software, demonstrating convincing compression performance but currently lacks real-time capabilities [30]. In contrast, Google’s Draco [13] offers low latency but exhibits inferior rate-distortion efficiency. Alternatively, range image-based methods [10, 15, 26, 32, 39, 48, 50] suffer from projection errors, which result in a loss of information [38] and may hinder the performance of reconstruction-related tasks [42].

In recent years, neural codecs [11, 16, 17, 22, 31, 35, 37, 44, 47] have garnered significant attention. While these methods present impressive rate-distortion performance, their space-time complexity makes them unusable for real-time LiDAR data compression and transmission. For ex-

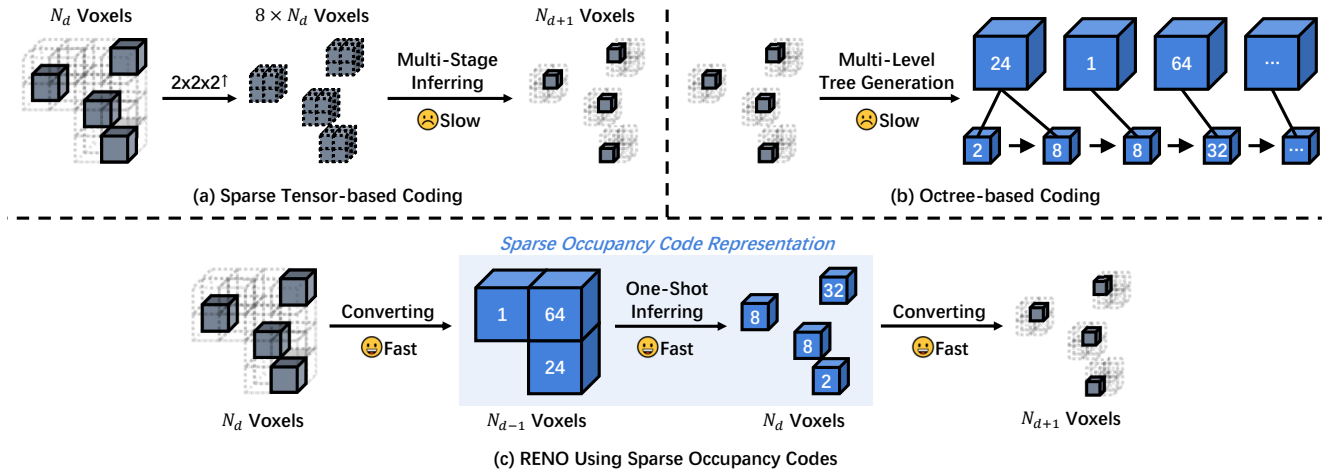


Figure 2. Comparison of learned LPCC pipelines. The refinement of point clouds from depth (or scale) d (with N_d voxels) to depth $d + 1$ (with N_{d+1} voxels) is employed as a toy example for better illustration. (a) Current sparse tensor-based methods predominantly employ a multi-stage inferring pipeline. However, the involved upsampling operation introduces $8 \times N_d$ voxels for neural network-based inference, leading to significant computational costs. (b) The octree-based method leverages the tree representation to obtain extensive contextual information but requires a time-intensive process for multi-level octree generation. (c) RENO introduces sparse occupancy codes to avoid multi-level tree generation and facilitate high-speed one-shot inferring, delivering real-time compression.

ample, one of the current state-of-the-art methods, Unicorn [37], demonstrates favorable complexity; however, it still takes approximately 2 seconds to encode one 14-bit LiDAR frame on an RTX 3090 GPU. This prompts the question: “Why do current neural codecs face runtime bottlenecks with 3D LiDAR point clouds, and how can we overcome these issues?”

In multiscale sparse tensor-based solutions [35, 37], the compression of current-scale voxels² involves the dyadic upscaling of (causally-available) lower-scale voxels to form proper contexts for entropy coding. Although Unicorn [37] grouped current-scale voxels to perform multi-stage computation to remove autoregressive processing, real-time compression remains challenging (see Fig. 2(a)). On the other hand, although octree models [16, 41] can use a node’s occupancy symbol to infer the occupancy status of its eight child nodes, the process of constructing the octree of each input point cloud is notably complex (see Fig. 2(b)). Some recent explorations [9, 22] attempted to improve computational efficiency by integrating octree and sparse tensor representations, but they did not radically solve the problem because of 1) pre-generating octree structure and 2) multi-stage processing using upscaled voxels (from lower depth).

We introduce RENO that employs the multiscale sparse tensor representation to skip time-consuming octree generation in Fig. 2(b) and proposes to compress 8-bit sparse occupancy codes in a one-shot manner at each scale (or depth) to avoid multi-stage processing as in Fig. 2(a). As a result, the compression of LiDAR point cloud geometry

is formulated as the compression of sparse occupancy code sequence scale by scale.

Sparse occupancy codes can be directly derived using fixed-weights sparse convolution along with dyadic down-scaling when generating multiscale sparse tensors. They carry the same categorical values (1–255) as the occupancy symbols in octree-structured nodes, which are used to explicitly indicate occupied child nodes in octree representation (i.e., now dyadically upscaled voxels at the following high scale), but they are *orderless* instead of tree-ordered in an octree model. Then, they are compressed with contexts conditioned on the available information (e.g., occupancy codes, occupied coordinates) from the lower scale.

The proposed RENO makes the following contributions:

- It is probably *the first* neural model to compress 3D LiDAR point cloud geometry in a real-time manner, which acts in concert with the spinning speed of popular LiDAR sensors.
- It also outperforms the latest LiDAR compression standard G-PCC, Draco, etc, owing to the cross-scale context modeling to compress the proposed sparse occupancy codes scale by scale.
- It is also a lightweight model with a size of merely 1 MB, making it attractive to industrial practitioners.

2. Related Works

Numerous studies have advanced the field of LiDAR Point Cloud Compression (LPCC). To appreciate the inherent sparsity of LiDAR point clouds, a given input frame has to be geometrically structured into trees, multiscale sparse

²Voxels or points refer to occupied coordinates in a point cloud frame.

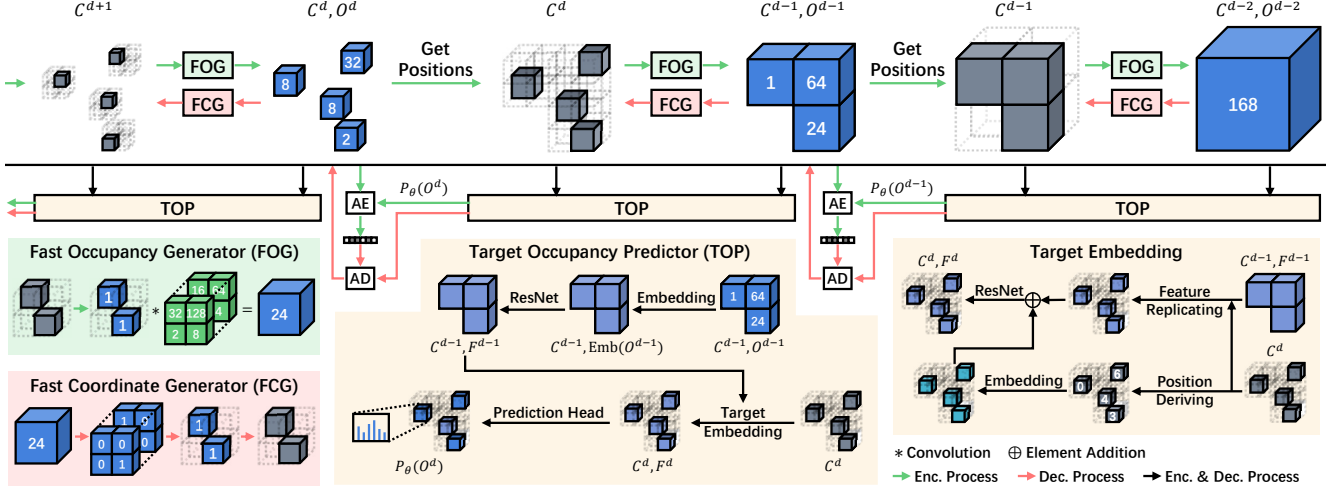


Figure 3. RENO. We identify that the real-time bottleneck of current neural codecs resides in two stages: preprocessing and neural inference. To surmount these obstacles, this approach endeavors to optimize efficiency by (i) minimizing preprocessing delays through the efficient acquisition of occupancy codes directly within sparse space via the developed Fast Occupancy Generator (FOG) and Fast Coordinate Generator (FCG); (ii) optimizing neural inference by efficiently embedding features from sparse occupancy codes to the next-level target positions, which prompted the development of the Target Occupancy Predictor (TOP).

tensors, or range images for context modeling.

Tree. One is the simple *kd-tree* [27], which has been used in Google’s Draco [13] for real-time compression. Another popular one is the *octree*, which was widely studied [3, 29, 40] and incorporated into the MPEG G-PCC standard [41]. G-PCC adopted heuristic rules to mine neighbors to form contexts for entropy coding, showing improved compression efficiency but a much slower processing speed than Draco.

More recently, OctSqueeze [16] and OctAttention [11] pioneered efforts by introducing learnable contextual models. Such a learning-based context modeling was subsequently advanced by the development of ECM-OPCC [17], EHEM [31], and others [7, 8], yielding noticeable progress of coding efficiency. Yet, generating an octree-structured point cloud for context modeling creates a notable runtime bottleneck.

Multiscale Sparse Tensor. Besides the octree representation, the multiscale sparse tensor formulation was introduced in SparsePCGC [35] and has been further refined in subsequent research endeavors (e.g., SparsePCGCv2 [43], Unicorn [37], etc.). However, pruning upsampled sub-voxels to effectively determine their occupancy statuses often relies on multi-stage processing, which is also time-consuming.

While certain approaches [9, 22] attempt to enhance computational efficiency by integrating octree-based occupancy codes with sparse tensor representations, these methods remain fundamentally limited by the abovementioned constraints.

Range Images. Alternatively, considering laser sen-

sor’s physical properties, the LiDAR point cloud frame can be projected to produce a 2D range image, which has consequently inspired the development of various range image-based compression methods [10, 15, 32, 39, 48, 50]. Nonetheless, projection-based approaches introduce significant degradation [42] and fail to provide high-fidelity reconstruction of point clouds.

3. Method

As shown in Fig. 3, RENO is built upon the multiscale sparse tensor representation [35, 37], in which scale-wise sparse tensors of point cloud geometry (occupied coordinates, or voxels), e.g., $\{\dots, C^d, C^{d-1}, \dots\}$, are progressively generated via dyadically downscaling³ from one scale depth to a lower one (e.g., d to $d-1$). Such a representation enables voxels to be processed directly in native Cartesian space, thereby avoiding the complexities associated with tree construction. A detailed illustration of the multiscale sparse tensor can be found in [35].

RENO further introduces the sparse occupancy code to strike for more efficiency. It is defined through the following state transitions:

$$C^d = (C^{d-1}, O^{d-1}) = \left(\left\{ \{c_i^{d-1}\}_{i=1}^{N_{d-1}}, \{o_i^{d-1}\}_{i=1}^{N_{d-1}} \right\} \right), \quad (1)$$

where $O^{d-1} = \{o_i^{d-1}\}_{i=1}^{N_{d-1}}$ contains the corresponding sparse occupancy code $o_i^{d-1} \in [1, 255]$ for each coordinates

³Dyadic down-/up-scaling is more or less the same as the octree squeezing/expanding [35].

c_i^{d-1} . N_{d-1} stands for the number of voxels at depth scale $d-1$.

As for the transformation defined Eq. (1), we have

- $C^d \rightarrow (C^{d-1}, O^{d-1})$ is to generate sparse occupancy codes O^{d-1} of C^d , which is fulfilled using Fast Occupancy Generator (FOG) along with the dyadic downscaling;
- $(C^{d-1}, O^{d-1}) \rightarrow C^d$ is the reconstruction of coordinates C^d at depth d from the coordinates C^{d-1} at depth $d-1$ and their occupancy codes O^{d-1} , which is implemented using Fast Coordinate Generator (FCG) along with dyadic upscaling.

In the end, the raw tensor of the input point cloud geometry C^D can be formulated as:

$$C^D = (((((C^0, O^0), O^1), O^2), \dots), O^{D-1}), \quad (2)$$

suggesting that C^D can be reconstructed losslessly by the initial state (C^0, O^0) and a sequence of sparse occupancy codes $\mathcal{O} = (O^1, O^2, \dots, O^{D-1})$ at different depth scales.

Thus, the compression of C^D is to compress the sparse occupancy code sequence \mathcal{O} . Specifically, we use a neural network - Target Occupancy Predictor (TOP) to form the probability mass function $P_\theta(\mathcal{O})$:

$$\begin{aligned} P_\theta(\mathcal{O}) &= \prod_{d=1}^{D-1} P_\theta(O^d | O^{<d}, C^0) \\ &= \prod_{d=1}^{D-1} P_\theta(O^d | O^{d-1}, C^{d-1}), \end{aligned} \quad (3)$$

Relevant tensors O^{d-1} and C^{d-1} are causally available priors from lower scale at depth $d-1$ in multiscale sparse representation framework, which are combined to exploit cross-scale correlations for context modeling. And, recalling the definition in (1), geometry coordinates at depth d , e.g., C^d , can be easily inferred using O^{d-1} and C^{d-1} . As a result, in our implementation (see (5)) to realize (3) using TOP, we explicitly embedded as the prior to compress O^d .

Then, given the true distribution $P(\mathcal{O})$, the optimization for the compression can be formulated using cross-entropy:

$$\theta^* \leftarrow \arg \min_{\theta} \mathbb{E}_{\mathcal{O} \sim P(\mathcal{O})} [-\log P_\theta(\mathcal{O})]. \quad (4)$$

3.1. Fast Occupancy Converters

In previous studies [11, 16, 17, 23, 31], octree-structured occupancy codes or symbols are derived by constructing the tree, which is time-consuming. Instead, we propose a Fast Occupancy Generator (FOG) to produce occupancy codes⁴ directly upon scale-wise sparse tensor of geometry coordinates, i.e., $(C^{d-1}, O^{d-1}) = \text{FOG}(C^d)$. Correspondingly, the Fast Coordinate Generator (FCG) is developed to

⁴We call them *Sparse Occupancy Codes* for convenience.

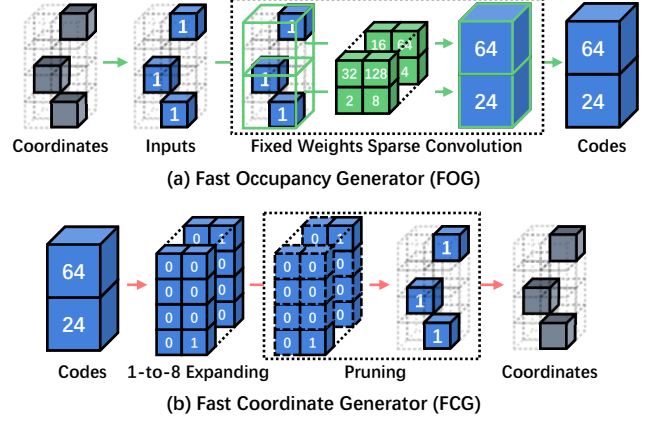


Figure 4. Illustrative implementation for Fast Occupancy Generator (FOG) and Fast Coordinate Generator (FCG).

convert sparse occupancy codes back into geometry coordinates, i.e., $C^d = \text{FCG}(C^{d-1}, O^{d-1})$.

Fast Occupancy Generator (FOG) is implemented using a sparse convolution with a kernel size of 2 and a stride of 2. Kernel’s weights are manually fixed using [1, 2, 4, 8, 16, 32, 64, 128].

As detailed in Fig. 4 (a), geometry coordinates of voxels are initially set to “1”, then convoluted to produce the corresponding occupancy codes for each group of eight inter-connected nodes. Following the discussions above, the sparse occupancy code is an integer, ranging from 1 to 255, explicitly indicating the occupancy status of the eight nodes mentioned above. Having a code for each group of eight interconnected nodes is similar to assigning an occupancy symbol during octree construction. As seen, such a process involves dyadic downscaling or octree squeezing to merge a group of eight nodes into a single one.

In practice, fixed-weights sparse convolution easily supports parallel acceleration, offering a much lighter load for efficient computing.

Fast Coordinates Generator (FCG) comprises the steps of “expanding” and “pruning”. As shown in Fig. 4 (b), each sparse occupancy code is first expanded into an 8-bit binary representation, with each bit corresponding to a distinct sub-node. Such a process involves the dyadic upscaling or octree expansion to split a voxel into eight connected nodes. Following this expansion, a pruning operation is instantly conducted to just retain nodes marked with “1” to form the coordinate tensor.

Next, we discuss how to compress the aforementioned sparse occupancy codes efficiently.

3.2. Target Occupancy Predictor

A neural network-based Target Occupancy Predictor (TOP) is proposed to effectively estimate the probability of sparse occupancy codes at each scale. Thus, (3) can be rewritten

as

$$P_\theta(O^d) = \text{TOP}(C^{d-1}, O^{d-1}, C^d), \quad (5)$$

where C^{d-1} and O^{d-1} represent the coordinates and occupancy codes of sparse tensor at depth $d-1$, respectively; C^d refers to the coordinate tensor at depth d , implying *target positions* of O^d ; $P_\theta(O^d)$ refers to the parametric probability distribution of O^d . Intuitively, the distribution can also be inferred only considering the target coordinates (i.e., $P_\theta(O^d) = \text{TOP}(C^d)$). Whereas this paper further introduces C^{d-1} and O^{d-1} to augment prior information from a lower scale, by which cross-scale correlations can effectively improve probability estimation.

Occupancy Feature Extraction. Considering that O^{d-1} constitute discrete values, we first utilize a naive embedding Emb to transform these codes into continuous vector representations, followed by a ResNet block that further characterizes neighborhood patterns to form aggregated features $F^{d-1} \in \mathbb{R}^{N^{d-1} \times \text{dim}}$, i.e.,

$$(C^{d-1}, F^{d-1}) = \text{ResNet}(C^{d-1}, \text{Emb}(O^{d-1})). \quad (6)$$

Subsequently, target embedding is devised to transfer features F^{d-1} from lower scale coordinates C^{d-1} to the target scale coordinates C^d , as illustrated in the subplot of TOP in Fig. 3.

Target Embedding. As illustrated in the subplot in Fig. 3, to enable efficient transfer of cross-scale features, the introduced target embedding consists of two steps: direct feature replication and relative position infusion.

In the first step, features from the previous scale are directly replicated to the corresponding sub-voxels of the current scale. Let $\tilde{F}^d = \{\tilde{f}_i^d\}_{i=1}^{N_d}$ indicate the replicated features of the current scale, then each feature vector \tilde{f}_i^d can be expressed as follows:

$$\tilde{f}_i^d = f_j^{d-1}, \quad \forall c_i^d \in \Lambda(c_j^{d-1}) \quad (7)$$

where $c_i^d \in C^d$, $c_j^{d-1} \in C^{d-1}$, and $f_j^{d-1} \in F^{d-1}$; specifically, $\Lambda(c_j^{d-1})$ represents the set of coordinates corresponding to the eight sub-voxels of c_j^{d-1} .

In the second step, the relative position is identified and embedded in the replicated features. Here, we leverage the widely used octant representation to characterize the position of the sub-voxels in relation to the parent voxel. Following (7), the octant $\delta_i^d \in \Delta^d$ of each coordinate $c_i^d \in C^d$ can be formulated as:

$$\delta_i^d = \sum_{k=1}^3 (c_i^d[k] - c_j^{d-1}[k]) \times 2^{k-1}, \quad \forall c_i^d \in \Lambda(c_j^{d-1}), \quad (8)$$

where $[k]$ represents of the k -th coordinate element, i.e., x , y , and z in this example. Subsequently, the octant is embedded to the replicated feature \tilde{F}^d , to produce the feature F^d on the target coordinates C^d :

$$\begin{aligned} (C^d, F^d) &= \text{ResNet}(C^d, \tilde{F}^d + \Delta F^d) \\ &= \text{ResNet}(C^d, \tilde{F}^d + \text{Emb}(\Delta^d)). \end{aligned} \quad (9)$$

Probability Prediction. Leveraging aggregated features F^d associated with target coordinates C^d , a one-stage inference is performed using a multilayer perceptron (MLP) and SoftMax layer to generate a 255-dimensional probability for the occupancy code in O^d , e.g.,

$$P_\theta(O^d) = \text{SoftMax}(\text{MLP}(F^d)). \quad (10)$$

Although directly predicting 8-bit codes is doable as in (10), our implementation has revealed that a bitwise two-stage strategy is preferable, not only showing an improvement of compression but also demonstrating better computational efficiency. This is because 1) predicting a 4-bit symbol is much easier than predicting an 8-bit one, not to mention that the last 4-bit symbol can also be conditionally predicted using the first 4-bit symbol; 2) transferring $(2 \times N \times 16)$ -element tensor of probabilities of 4-bit symbols from GPU to CPU for entropy coding significantly reduces the memory bandwidth by a factor of ≈ 8 when transferring $(N \times 255)$ -element tensor of probabilities for original 8-bit symbols. Here, we assume the entropy coding on the CPU as most existing works.

As for the proposed bitwise two-stage scheme, a given 8-bit occupancy code in O^d is segmented into the first 4-bit sub-codes S_1^d and the last 4-bit sub-codes S_2^d :

$$P_\theta(O^d) = P_\theta(S_2^d, S_1^d) = P_\theta(S_2^d | S_1^d) P_\theta(S_1^d). \quad (11)$$

Notably, the compression process is initiated with S_1^d :

$$P_\theta(S_1^d) = \text{SoftMax}(\text{MLP}(F^d)), \quad (12)$$

where F^d refers to the inherited features of the target coordinates, as demonstrated in Eq. (9). Then, S_1^d will be used as a priori knowledge for S_2^d to assist its encoding, i.e.,

$$P_\theta(S_2^d | S_1^d) = \text{SoftMax}(\text{MLP}(F^d + \text{Emb}(S_1^d))). \quad (13)$$

3.3. Loss Function

Since this paper focuses on the lossless compression of sparse occupancy codes, its loss function is to optimize the cross-entropy as in (4), i.e., $\mathcal{L} = \mathbb{E}_{O \sim P(O)} [-\log P_\theta(O)] = \sum_{d=1}^{D-1} \mathbb{E}_{O^d \sim P(O^d)} [-\log P_\theta(O^d)]$.

4. Experiments and Discussions

4.1. Experimental Setup

4.1.1. Dataset

Experiments are performed using two widely recognized datasets, namely KITTI [12] and Ford [28]. First, compression efficiency evaluation includes rate-distortion performance, qualitative visualization, and computational complexity. Then, the downstream vision task, i.e., 3D object detection, is fulfilled to examine the effectiveness of machine visions on compressed LiDAR data.

Table 1. Quantitative BD-BR gains of RENO over other methods are reported. The encoding/decoding time is collected for 12/14 bit ($\pm 3.2\text{cm}/\pm 8\text{mm}$ precision) KITTI samples.

Dataset	Metric	RTST	R-PCC	Draco	G-PCC	RENO
KITTI	D1 (%)	-90.66	-84.80	-48.34	-12.26	-
	D2 (%)	-70.04	-60.17	-48.30	-12.23	-
Ford	D1 (%)	-	-82.54	-45.01	-12.50	-
	D2 (%)	-	-68.34	-44.97	-12.69	-
12 bit	Enc (s)	0.046	0.074	0.065	0.564	0.052
	Dec (s)	0.008	0.048	0.028	0.174	0.050
14 bit	Enc (s)	-	-	0.075	0.973	0.095
	Dec (s)	-	-	0.032	0.343	0.090

KITTI [12] comprises 14,999 point clouds generated by a Velodyne HDL-64E laser scanner. We adhere to the official data split, which contains 3,712 point clouds for training, 3,769 point clouds for validation, and 7,518 point clouds for testing.

Ford [28] consists of three sequences of 1,500 LiDAR scans used for MPEG standardization. Following the common test condition, sequence 01 is used for training, while sequences 02 and 03 are reserved for evaluation.

4.1.2. Implementation

RENO uses Python 3.9 and PyTorch 1.10 for implementation. It leverages TorchSparse++ [33] for efficient sparse convolution. The Adam optimizer [18] is employed with an initial learning rate of $5e-4$ and a batch size of 1. The model is trained for 100,000 steps, with training samples quantized to 16-bit precision. All experiments are conducted on an Intel Xeon Silver 4314 CPU and one NVIDIA GeForce RTX 3090 GPU. Due to the variability in implementation details of different methods (e.g., CPU vs. GPU), the runtime comparison is intended to provide an intuitive reference of computational complexity.

4.1.3. Benchmarking Baselines

Extensive comparisons are performed: First, since this work focuses on real-time compression, we choose three real-time compressors: Draco [13], RPCC [39] and RTST [10]. Draco [13] is a tree-based solution, while RPCC [39] and RTST [10] uses range images to fulfill the purposes. Second, the latest (but non-real-time) G-PCCv23 [41] standard is also included to justify the advantage of RENO’s compression performance. Additional comparison to existing learning-based LPCC like Unicorn [37], EHEM [31], etc. will be provided in the supplemental material.

4.2. Comparative Studies

4.2.1. Rate-Distortion Performance

As evidenced in Tab. 1 and Fig. 5, RENO consistently outperforms the competing methods across the entire bitrate

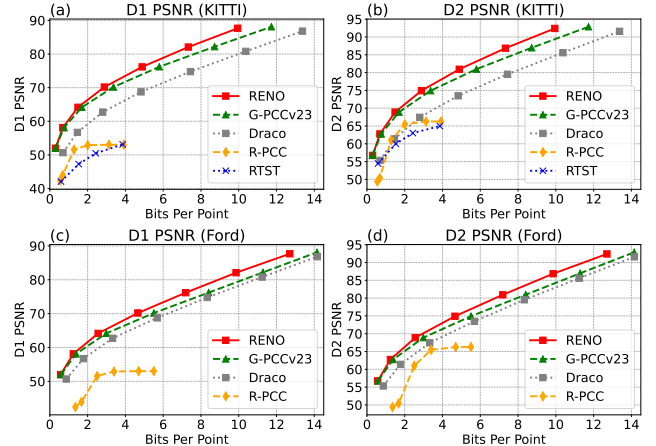


Figure 5. Rate-distortion performance comparison on KITTI (the first row) and Ford (the second row).

range in both point-to-point (D1) and point-to-plane (D2) metrics, showcasing its superiority. Although G-PCCv23 achieves convincing rate-distortion performance, it lacks real-time capabilities due to the intricate rules employed for entropy coding and non-optimized reference software implementation [41]. On the other hand, the performances of real-time methods (e.g., Draco, R-PCC, and RTST) are noticeably inferior. Particularly, R-PCC and RTST, which adopt range image representation to facilitate low-latency compression, support only a narrow bitrate range and suffer from poor reconstruction fidelity. This limitation is due to the significant distortion introduced by the 3D to 2D projection to obtain range images [42].

4.2.2. Computational complexity

The encoding and decoding times in Tab. 1 further support RENO’s real-time capability. For 12-bit LiDAR point clouds, RENO achieves encoding in 0.052 seconds and decoding in 0.050 seconds, closely matching or even surpassing the performance of other rules-based real-time methods. In the case of 14-bit samples, RENO continues to achieve real-time latency on average (e.g., ten frames per second), which meets the typical frequency requirements of LiDAR sensors for data collection. It is important to recognize that, owing to the specificity inherent in range image-based methods, these approaches are unable to attain standard reconstruction for a particular level of bit accuracy. Therefore, the runtimes of RPCC and RTST at 12 bits, as shown in Tab. 1, are reported under low bit rate conditions (approximately 3 bits per point) for reference. Additionally, their runtimes at 14 bits are not applicable due to their inability to attain a comparable level of accuracy.

4.2.3. Qualitative Visualization

Figure 6 visualizes the reconstructed samples of various methods in both low-bitrate and high-precision scenarios,

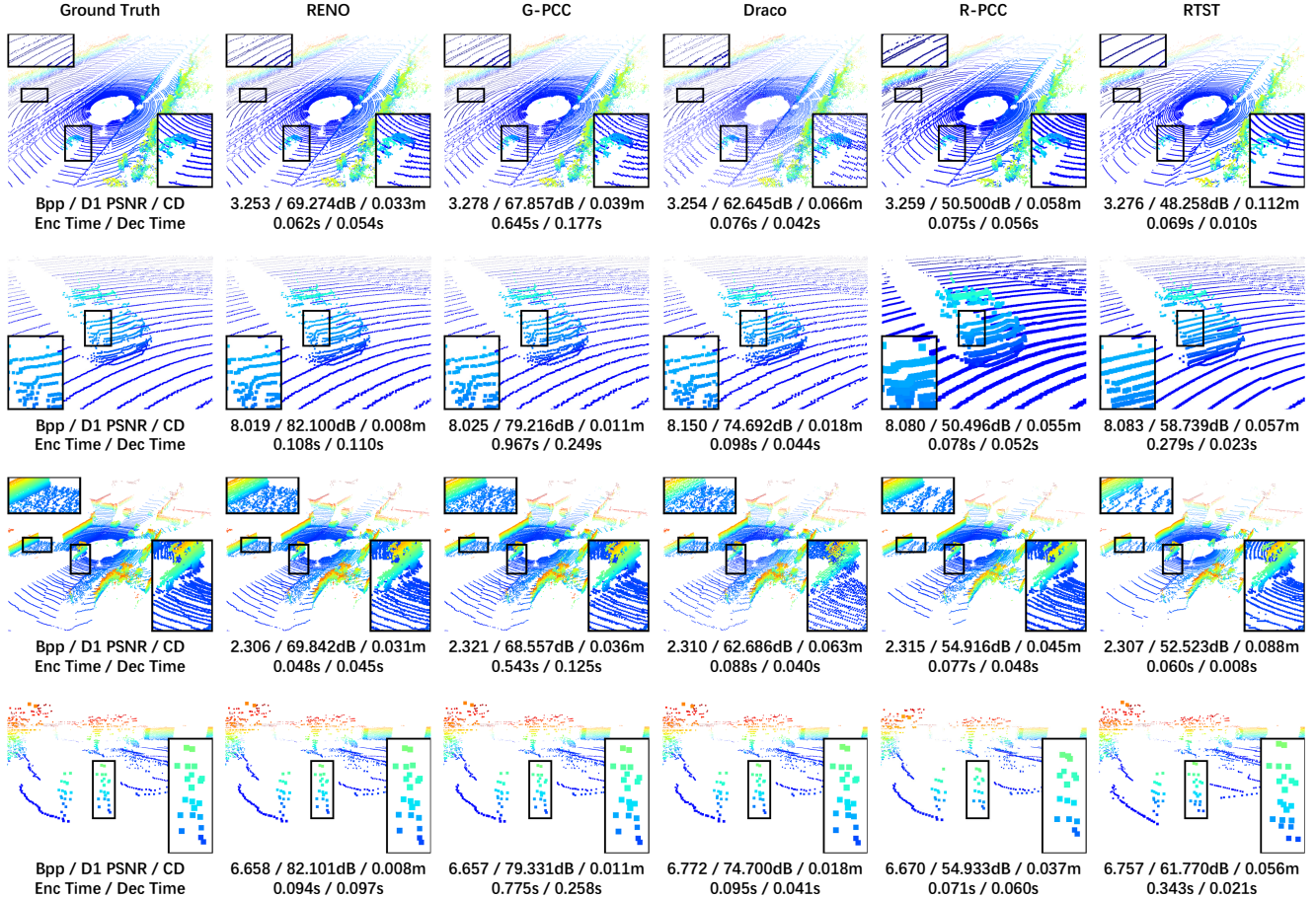


Figure 6. Qualitative visualization. CD refers to Chamfer Distance. The first and third rows indicate the compression results at lower bit rates, while the second and fourth rows indicate compression results at higher bit rates with lower distortion. The color indicates the height above ground, ranging from blue (low) to red (high).

using two KITTI point clouds as examples. It is evident that our method achieves significantly superior reconstruction quality compared to other real-time methods. For instance, RENO effectively reconstructs the scan strips and vehicle contours at low bit rate conditions. In contrast, Draco appears blurry, and both RTST and R-PCC exhibit a significant lack of scan integrity. At high bit rates, RENO presents an accurate point reconstruction, providing a Chamfer Distance of only 8 mm, which is less than half of Draco’s. We can also observe that, despite a substantial bitrate budget, range image-based methods still struggle to reconstruct points accurately, which confirms the significant distortion caused by 2D projection.

4.2.4. Downstream Task Evaluation

Criticism often arises: Why must we compress LiDAR if we can perform vision tasks on front devices using raw captures? One reason is that we can store on-device LiDAR for late (autopilot) simulation purposes. On the other hand, efficient LiDAR can potentially enable device-to-device or

vehicle-to-vehicle sharing with rich LiDAR information for collaborative decision-making. To fulfill it, we must assure the same task accuracy when using a compressed LiDAR sequence as when using uncompressed raw data.

We thus evaluate the performance of a prevalent 3D object detection task using decoded point clouds generated by various real-time LPCCs. We utilize the CenterPoint [46] as the detector, which is trained on raw data, and apply it directly to decoded point clouds. As seen from Fig. 7 (a)-(d), our approach exhibits substantially superior precision to Draco and exhibits enhanced stability relative to the range image-based baseline (e.g., R-PCC), especially under low bitrate conditions. G-PCC also demonstrates strong detection performance; however, as illustrated in Fig. 7 (e) and (f), this performance is accompanied by a significant coding latency, rendering it unsuitable for real-time applications. As demonstrated in Fig. 7 (d), on average, a 12-bit point cloud is sufficient to attain an accuracy close to that of raw LiDAR scan (65.64 mAP vs. 65.97 mAP), and our method

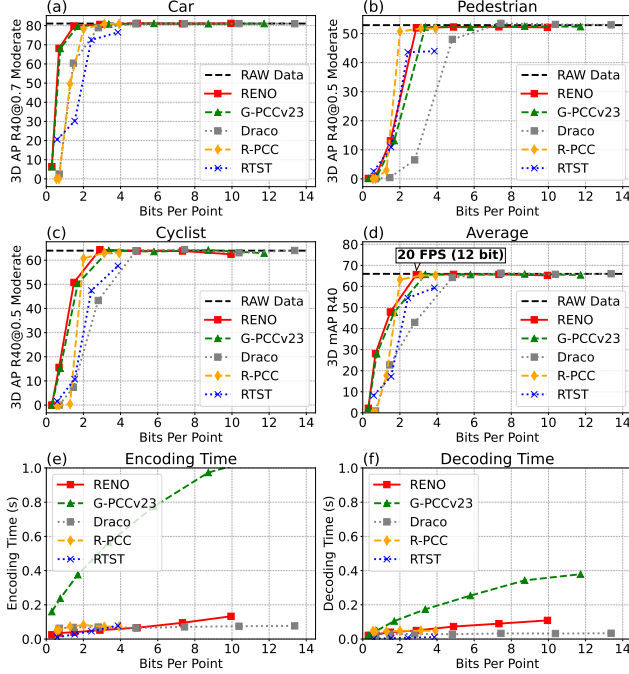


Figure 7. 3D object detection on the KITTI dataset.

Table 2. Target embedding vs. target convolution. BD-BR gain is against G-PCCv23 in D1 metric. “w/o Both” means the omission of scale-wise feature inheritance. The network inference time for 14 bit KITTI point clouds is reported.

Module	Implementation	BD-BR (%)	Inference (s)
w/o Both	MinkowskiEngine [5]	-6.05	0.045
w/o Both	TorchSparse++ [33]	-6.06	0.024
w/ TargetConv	MinkowskiEngine [5]	-8.53	0.101
w/ TargetConv	TorchSparse++ [33]	-	-
w/ TargetEmb	MinkowskiEngine [5]	-12.24	0.071
w/ TargetEmb	TorchSparse++ [33]	-12.26	0.035

Table 3. Time consumption for Fast Occupancy Generator (FOG), Neural Network Inference (NN), and Arithmetic Encoding (AE).

	BD-BR (%)	FOG (s)	NN (s)	AE (s)	Total (s)
One-Stage	-11.45	0.008	0.036	0.102	0.146
Two-Stage	-12.26	0.008	0.035	0.052	0.095

can achieve a processing speed of 20 frames per second under 12-bit condition.

4.3. Ablation Studies

Target Embedding vs. Target Convolution. In Target Occupancy Predictor (TOP), we employ a target embedding (TargetEmb) to inherit features from the lower scale. Alternatively, we can apply the “convolution on target coordinates” operation [2, 36], referred to as target convolution

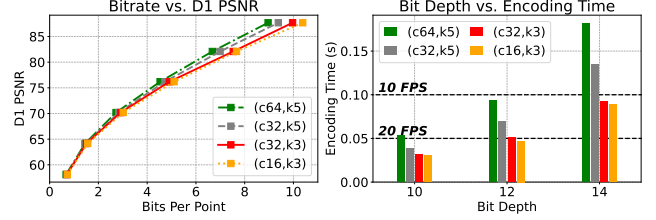


Figure 8. Analysis on channel and kernel size of our neural network. “(c64, k5)” denotes the model with 64 channels and a kernel size of 5, with other notations following a similar pattern.

(TargetConv), to transfer the features of the previous scale to the current scale. However, TargetConv is not supported by TorchSparse++ but by MinkowskiEngine platform.

Table 2 presents ablation experiments comparing both modules, where we reimplement our method on the MinkowskiEngine [5] library for the support of target convolution operation. As seen, the target embedding significantly outperforms target convolution in both inference speed and rate-distortion performance

Channel and Kernel Size Analysis. Intuitively, increasing the number of channels and the kernel size contributes to a higher compression ratio, but at the expense of increased inference latency. Figure 8 shows the results of different channels and kernel sizes. This paper adopts a “(c32, k3)” configuration to achieve a balance between performance and latency on our current platform. Nevertheless, with the availability of more powerful hardware, the neural model can be scaled up to achieve better compression ratios.

Bitwise Two-Stage Coding. The bitwise two-stage coding scheme is introduced to encode the occupancy codes in a two-stage manner. To validate its efficacy, a one-stage baseline is established for comparison. The results presented in Table 3 demonstrate that the bitwise two-stage coding scheme significantly reduces the latency of arithmetic coding operations, thereby facilitating real-time compression.

Please refer to our supplementary material for more ablation studies and discussions.

5. Conclusion

This paper presents RENO - a LiDAR coder built upon multiscale sparse representation. At each scale, it compresses sparse occupancy codes to infer voxels’ occupancy in a one-shot manner, where the derivation of sparse occupancy codes utilizes fixed-weights sparse convolution without resorting to complex octree construction, and the compression of these codes exploits cross-scale correlations through conditional coding. RENO offers superior performance at a real-time compression speed, which is attractive for applications like autonomous machinery to save and exchange instantly captured LiDAR data for better decision-making.

6. Acknowledgement

This work was supported in part by the Key Project of Jiangsu Science and Technology Department under Grant BK20243038, and in part by the Key Project of the National Natural Science Foundation of China under Grant 62431011. The authors would like to express their sincere gratitude to the Interdisciplinary Research Center for Future Intelligent Chips (Chip-X) and Yachen Foundation for their invaluable support.

References

- [1] Rashid Abbasi, Ali Kashif Bashir, Hasan J Alyamani, Farhan Amin, Jaehyeok Doh, and Jianwen Chen. Lidar point cloud compression, processing and learning for autonomous driving. *IEEE Transactions on Intelligent Transportation Systems*, 24(1):962–979, 2022. 1
- [2] Anique Akhtar, Zhu Li, and Geert Van der Auwera. Inter-frame compression for dynamic point cloud geometry coding. *IEEE Transactions on Image Processing*, 2024. 8
- [3] Bhaskar Anand, Vivek Barsaiyan, Mrinal Senapati, and Pachamuthu Rajalakshmi. Real time lidar point cloud compression and transmission for intelligent transportation system. In *2019 IEEE 89th Vehicular Technology Conference (VTC2019-Spring)*, pages 1–5. IEEE, 2019. 3
- [4] Li Chen, Penghao Wu, Kashyap Chitta, Bernhard Jaeger, Andreas Geiger, and Hongyang Li. End-to-end autonomous driving: Challenges and frontiers. *IEEE Transactions on Pattern Analysis and Machine Intelligence*, pages 1–20, 2024. 1
- [5] Christopher Choy, JunYoung Gwak, and Silvio Savarese. 4d spatio-temporal convnets: Minkowski convolutional neural networks. In *Proceedings of the IEEE Conference on Computer Vision and Pattern Recognition*, pages 3075–3084, 2019. 8
- [6] Jiaxun Cui, Hang Qiu, Dian Chen, Peter Stone, and Yuke Zhu. Coopernaut: End-to-end driving with cooperative perception for networked vehicles. In *Proceedings of the IEEE/CVF Conference on Computer Vision and Pattern Recognition*, pages 17252–17262, 2022. 1
- [7] Mingyue Cui, Junhua Long, Mingjian Feng, Boyang Li, and Huang Kai. Octformer: Efficient octree-based transformer for point cloud compression with local enhancement. In *Proceedings of the AAAI Conference on Artificial Intelligence*, pages 470–478, 2023. 3
- [8] Mingyue Cui, Mingjian Feng, Junhua Long, Daosong Hu, Shuai Zhao, and Kai Huang. A du-octree based cross-attention model for lidar geometry compression. In *2024 IEEE International Conference on Robotics and Automation (ICRA)*, pages 3796–3802. IEEE, 2024. 3
- [9] Tingyu Fan, Linyao Gao, Yiling Xu, Dong Wang, and Zhu Li. Multiscale latent-guided entropy model for lidar point cloud compression. *IEEE Transactions on Circuits and Systems for Video Technology*, 33(12):7857–7869, 2023. 2, 3
- [10] Yu Feng, Shaoshan Liu, and Yuhao Zhu. Real-time spatio-temporal lidar point cloud compression. In *2020 IEEE/RSJ international conference on intelligent robots and systems (IROS)*, pages 10766–10773. IEEE, 2020. 1, 3, 6
- [11] Chunyang Fu, Ge Li, Rui Song, Wei Gao, and Shan Liu. Octtattention: Octree-based large-scale contexts model for point cloud compression. In *Proceedings of the AAAI conference on artificial intelligence*, pages 625–633, 2022. 1, 3, 4
- [12] Andreas Geiger, Philip Lenz, and Raquel Urtasun. Are we ready for autonomous driving? the kitti vision benchmark suite. In *2012 IEEE conference on computer vision and pattern recognition*, pages 3354–3361. IEEE, 2012. 5, 6
- [13] Google. Draco: 3d data compression, 2018. 1, 3, 6
- [14] Xiaoshuai Hao, Ruikai Li, Hui Zhang, Dingzhe Li, Rong Yin, Sangil Jung, Seung-In Park, ByungIn Yoo, Haimei Zhao, and Jing Zhang. Mapdistill: Boosting efficient camera-based hd map construction via camera-lidar fusion model distillation. *arXiv preprint arXiv:2407.11682*, 2024. 1
- [15] Jin Heo, Christopher Phillips, and Ada Gavrilovska. Flicr: A fast and lightweight lidar point cloud compression based on lossy ri. In *2022 IEEE/ACM 7th Symposium on Edge Computing (SEC)*, pages 54–67. IEEE, 2022. 1, 3
- [16] Lila Huang, Shenlong Wang, Kelvin Wong, Jerry Liu, and Raquel Urtasun. Octsqueeze: Octree-structured entropy model for lidar compression. In *Proceedings of the IEEE/CVF conference on computer vision and pattern recognition*, pages 1313–1323, 2020. 1, 2, 3, 4
- [17] Yiqi Jin, Ziyu Zhu, Tongda Xu, Yuhuan Lin, and Yan Wang. Ecm-opcc: Efficient context model for octree-based point cloud compression. In *ICASSP 2024-2024 IEEE International Conference on Acoustics, Speech and Signal Processing (ICASSP)*, pages 7985–7989. IEEE, 2024. 1, 3, 4
- [18] Diederik P Kingma. Adam: A method for stochastic optimization. *arXiv preprint arXiv:1412.6980*, 2014. 6
- [19] Ge Li, Wei Gao, and Wen Gao. Mpeg geometry-based point cloud compression (g-pcc) standard. In *Point Cloud Compression: Technologies and Standardization*, pages 135–165. Springer, 2024. 1
- [20] Zhicheng Liang et al. Fumos: Neural compression and progressive refinement for continuous point cloud video streaming. *IEEE TVCG*, 2024. 2
- [21] Shaoshan Liu, Bo Yu, Jie Tang, Yuhao Zhu, and Xue Liu. Communication challenges in infrastructure-vehicle cooperative autonomous driving: A field deployment perspective. *IEEE Wireless Communications*, 29(4):126–131, 2022. 1
- [22] Muhammad Asad Lodhi, Jiahao Pang, and Dong Tian. Sparse convolution based octree feature propagation for lidar point cloud compression. In *ICASSP 2023 - 2023 IEEE International Conference on Acoustics, Speech and Signal Processing (ICASSP)*, pages 1–5, 2023. 1, 2, 3
- [23] Ao Luo, Linxin Song, Keisuke Nonaka, Kyohei Unno, Heming Sun, Masayuki Goto, and Jiro Katto. Scp: Spherical-coordinate-based learned point cloud compression. In *Proceedings of the AAAI Conference on Artificial Intelligence*, pages 3954–3962, 2024. 4
- [24] Jiageng Mao, Shaoshuai Shi, Xiaogang Wang, and Hongsheng Li. 3d object detection for autonomous driving: A comprehensive survey. *International Journal of Computer Vision*, 131(8):1909–1963, 2023. 1
- [25] Ziliang Miao, Buwei He, Wenya Xie, Wenquan Zhao, Xiao Huang, Jian Bai, and Xiaoping Hong. Coarse-to-fine hybrid

- 3d mapping system with co-calibrated omnidirectional camera and non-repetitive lidar. *IEEE Robotics and Automation Letters*, 8(3):1778–1785, 2023. 1
- [26] Fabrizio Nenci, Luciano Spinello, and Cyrill Stachniss. Effective compression of range data streams for remote robot operations using h. 264. In *2014 IEEE/RSJ International Conference on Intelligent Robots and Systems*, pages 3794–3799. IEEE, 2014. 1
- [27] Salvador Pacheco-Gutierrez, Ipek Caliskanelli, and Robert Skilton. Point cloud compression and transmission for remote handling applications. *J. Softw.*, 16:14–23, 2021. 3
- [28] Gaurav Pandey, James R McBride, and Ryan M Eustice. Ford campus vision and lidar data set. *The International Journal of Robotics Research*, 30(13):1543–1552, 2011. 5, 6
- [29] Radu Bogdan Rusu and Steve Cousins. 3d is here: Point cloud library (pcl). In *2011 IEEE international conference on robotics and automation*, pages 1–4. IEEE, 2011. 3
- [30] Cristiano Santos, Leandro Tavares, Eduardo Costa, Gustavo Rehbein, Guilherme Corrêa, and Marcelo Porto. Coding efficiency and complexity analysis of the geometry-based point cloud encoder. In *2024 IEEE 15th Latin America Symposium on Circuits and Systems (LASCAS)*, pages 1–5. IEEE, 2024. 1
- [31] Rui Song, Chunyang Fu, Shan Liu, and Ge Li. Efficient hierarchical entropy model for learned point cloud compression. In *Proceedings of the IEEE/CVF Conference on Computer Vision and Pattern Recognition*, pages 14368–14377, 2023. 1, 3, 4, 6
- [32] Nikolaos Stathoulopoulos, Mario AV Saucedo, Anton Koval, and George Nikolakopoulos. Recnet: An invertible point cloud encoding through range image embeddings for multi-robot map sharing and reconstruction. *arXiv preprint arXiv:2402.02192*, 2024. 1, 3
- [33] Haotian Tang, Shang Yang, Zhijian Liu, Ke Hong, Zhongming Yu, Xiuyu Li, Guohao Dai, Yu Wang, and Song Han. Torchsparse++: Efficient training and inference framework for sparse convolution on gpus. In *IEEE/ACM International Symposium on Microarchitecture (MICRO)*, 2023. 6, 8
- [34] Guangming Wang, Xinrui Wu, Shuyang Jiang, Zhe Liu, and Hesheng Wang. Efficient 3d deep lidar odometry. *IEEE Transactions on Pattern Analysis and Machine Intelligence*, 45(5):5749–5765, 2022. 1
- [35] Jianqiang Wang, Dandan Ding, Zhu Li, Xiaoxing Feng, Chuntong Cao, and Zhan Ma. Sparse tensor-based multiscale representation for point cloud geometry compression. *IEEE Transactions on Pattern Analysis and Machine Intelligence*, 45(7):9055–9071, 2022. 1, 2, 3
- [36] Jianqiang Wang, Dandan Ding, Hao Chen, and Zhan Ma. Dynamic point cloud geometry compression using multiscale inter conditional coding. *arXiv preprint arXiv:2301.12165*, 2023. 8
- [37] Jianqiang Wang, Ruixiang Xue, Jiaxin Li, Dandan Ding, Yi Lin, and Zhan Ma. A versatile point cloud compressor using universal multiscale conditional coding – part i: Geometry. *IEEE Transactions on Pattern Analysis and Machine Intelligence*, pages 1–18, 2024. 1, 2, 3, 6
- [38] Li Wang, Xinyu Zhang, Ziyang Song, Jiangfeng Bi, Guoxin Zhang, Haiyue Wei, Liyao Tang, Lei Yang, Jun Li, Caiyan Jia, et al. Multi-modal 3d object detection in autonomous driving: A survey and taxonomy. *IEEE Transactions on Intelligent Vehicles*, 8(7):3781–3798, 2023. 1
- [39] Sukai Wang, Jianhao Jiao, Peide Cai, and Lujia Wang. R-pcc: A baseline for range image-based point cloud compression. In *2022 International Conference on Robotics and Automation (ICRA)*, pages 10055–10061. IEEE, 2022. 1, 3, 6, 2
- [40] Zhecheng Wang, Shuai Wan, and Lei Wei. Optimized octree codec for geometry-based point cloud compression. *Signal, Image and Video Processing*, 18(1):761–772, 2024. 3
- [41] MPEG 3D Graphics WG 7 and Haptics Coding. G-pcc 2nd edition codec description. *ISO/IEC JTC 1/SC 29/WG 7*, 2023. 1, 2, 3, 6
- [42] Tao Wu, Hao Fu, Bokai Liu, Hanzhang Xue, Ruike Ren, and Zhiming Tu. Detailed analysis on generating the range image for lidar point cloud processing. *Electronics*, 10(11):1224, 2021. 1, 3, 6
- [43] Ruixiang Xue, Jianqiang Wang, and Zhan Ma. Efficient lidar point cloud geometry compression through neighborhood point attention. *arXiv preprint arXiv:2208.12573*, 2022. 3, 1
- [44] Ruixiang Xue, Jiaxin Li, Tong Chen, Dandan Ding, Xun Cao, and Zhan Ma. Neri: Implicit neural representation of lidar point cloud using range image sequence. In *ICASSP 2024-2024 IEEE International Conference on Acoustics, Speech and Signal Processing (ICASSP)*, pages 8020–8024. IEEE, 2024. 1
- [45] Bochun Yang, Zijun Li, Wen Li, Zhipeng Cai, Chenglu Wen, Yu Zang, Matthias Muller, and Cheng Wang. Lisa: Lidar localization with semantic awareness. In *Proceedings of the IEEE/CVF Conference on Computer Vision and Pattern Recognition*, pages 15271–15280, 2024. 1
- [46] Tianwei Yin, Xingyi Zhou, and Philipp Krahenbuhl. Center-based 3d object detection and tracking. In *Proceedings of the IEEE/CVF conference on computer vision and pattern recognition*, pages 11784–11793, 2021. 7
- [47] Kang You, Kai Liu, Li Yu, Pan Gao, and Dandan Ding. Pointsoup: High-performance and extremely low-decoding-latency learned geometry codec for large-scale point cloud scenes. In *Proceedings of the Thirty-Third International Joint Conference on Artificial Intelligence, IJCAI-24*, pages 5380–5388. International Joint Conferences on Artificial Intelligence Organization, 2024. Main Track. 1
- [48] Lili Zhao, Kai-Kuang Ma, Xuhu Lin, Wenyi Wang, and Jianwen Chen. Real-time lidar point cloud compression using bi-directional prediction and range-adaptive floating-point coding. *IEEE Transactions on Broadcasting*, 68(3):620–635, 2022. 1, 3
- [49] Xingguang Zhong, Yue Pan, Cyrill Stachniss, and Jens Behley. 3d lidar mapping in dynamic environments using a 4d implicit neural representation. In *Proceedings of the IEEE/CVF Conference on Computer Vision and Pattern Recognition*, pages 15417–15427, 2024. 1
- [50] Xuanyu Zhou, Charles R Qi, Yin Zhou, and Dragomir Anguelov. Riddle: Lidar data compression with range image

deep delta encoding. In *Proceedings of the IEEE/CVF Conference on Computer Vision and Pattern Recognition*, pages 17212–17221, 2022. [1](#), [3](#)

RENO: Real-Time Neural Compression for 3D LiDAR Point Clouds

Supplementary Material

7. Overview

This appendix provides supplementary comparisons and discussions to complement the manuscript. Section 8 compares our approach with learning-based methods, while Sec. 9 presents additional ablation studies. Implementation details are discussed in Sec. 10, and more visualizations are provided in Sec. 11. All experiments in this appendix are conducted on an Intel Xeon Platinum 8352V CPU and one RTX 4090 GPU.

8. Comparison with Learning-based Methods

In this section, we provide a detailed comparison of RENO with representative learning-based methods: EHEM [31] and Unicorn [37]. EHEM is recognized as the most prominent and high-performing model among tree-based approaches [11, 16, 17, 31], while Unicorn exemplifies the latest and most representative sparse tensor-based models [35, 37, 43]. Table 4 shows the rate distortion performance of different methods, where RENO-L represents the large version of RENO, which increases the number of channels from 32 to 128 and the kernel size from 3 to 5. Table 5 provides detailed encoding time for various methods applied to 12-bit and 14-bit point clouds, where the first frame in SemanticKITTI sequence 11 is used for test.

- It can be observed that EHEM demonstrates the highest rate-distortion performance (note that the BD-BR of EHEM is directly cited from their paper and is presented for reference only); however, this comes at the cost of substantial time consumption. Its preprocessing stage demands significantly more time to construct the tree and prepare contextual information, ultimately undermining its real-time applicability.
- In contrast, Unicorn performs inference directly within the sparse tensor domain, effectively minimizing preprocessing overhead. However, its reliance on the upsampling-based inference framework results in a substantially prolonged neural network computation time. While the inference speed of the network can be enhanced using 1-stage inference, Unicorn¹ fails to achieve substantial speed improvements (as it still necessitates the introduction of a large number of voxels via deconvolution) and results in a significant degradation in performance.

9. Additional Ablation Study

CPU vs. GPU Arithmetic Coding. This paper employs a bitwise two-stage coding strategy to accelerate the

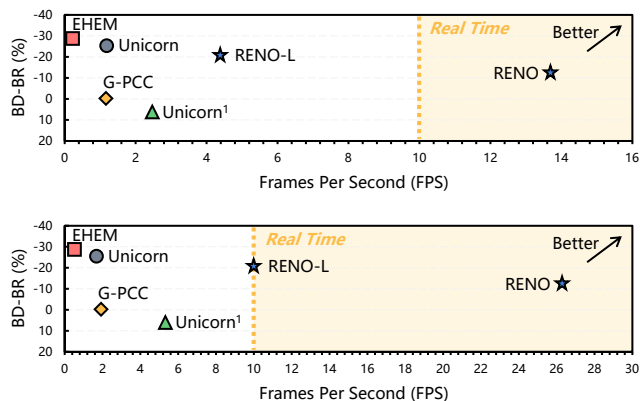


Figure 9. Comparison with the learning-based methods EHEM and Unicorn. The encoding speeds are reported separately for 14-bit precision (top) and 12-bit precision (bottom). Unicorn¹ refers to the one-stage configuration of the Unicorn model. G-PCC serves as the anchor.

Table 4. Rate-distortion comparison with learning-based methods on SemanticKITTI. BD-BR refers to the BD-BR gain over G-PCCv23 in D1 metric. Unicorn¹ denotes the one-stage configuration of the Unicorn model.

Method	EHEM	Unicorn	Unicorn ¹	RENO-L	RENO
BD-BR (%)	-28.89	-25.62	+6.56	-20.63	-12.47

Table 5. Encoding time comparison. Preprocessing (Prep), neural network inference (NN), and arithmetic encoding (AE) time are independently reported for detailed comparison. D refers to the bit depth of reconstructed point clouds. For sparse tensor-based methods (e.g., Unicorn, Unicorn¹, RENO-L, and RENO), the time spent on dyadic downscaling is reported as preprocessing.

Method	$D=12$ (s)				$D=14$ (s)			
	Prep	NN	AE	Total	Prep	NN	AE	Total
EHEM	0.463	0.427	0.297	1.187	1.796	1.385	1.233	4.414
Unicorn	0.003	0.565	0.030	0.598	0.003	0.772	0.074	0.849
Unicorn ¹	0.003	0.163	0.021	0.187	0.003	0.336	0.063	0.402
RENO-L	0.006	0.080	0.014	0.100	0.007	0.184	0.037	0.228
RENO	0.006	0.018	0.014	0.038	0.007	0.028	0.038	0.073

arithmetic coding process, leveraging the Torchac⁵ library, which operates on the CPU. An alternative acceleration strategy involves dividing symbols into packets for parallel coding directly on the GPU, an approach implemented in GPUAC⁶. Here, we performed ablation experiments for both methods, and the results are shown in Tab. 6. It should

⁵<https://github.com/fab-jul/torchac>

⁶<https://github.com/zb12138/GPUAC>

Table 6. Comparison of arithmetic coding implementations. The first frame in the SemanticKITTI sequence 11 is used for testing. Encoding time for different bit depths D are reported.

Module	Library	$D=12$		$D=14$	
		Time (s)	Bitrate	Time (s)	Bitrate
One-Stage	GPUAC	0.065	2.24	0.096	6.56
Two-Stage	GPUAC	0.064	2.25	0.093	6.55
One-Stage	Torchac	0.017	2.27	0.102	6.58
Two-Stage	Torchac	0.014	2.28	0.038	6.57

be noted that an independent arithmetic encoding process is conducted for each scale, and the reported time represents the accumulated arithmetic encoding time across all scales. The default packet size of 8192 is used when implementing GPUAC. As observed, GPUAC provides a slight speedup over the naive one-stage approach only at higher bitrates ($D=14$); however, this performance improvement is considerably inferior compared to the proposed bitwise decomposition strategy. At lower bitrates ($D=12$), GPUAC performs significantly slower, as the number of symbols is relatively small, and the CPU is sufficiently capable of processing the data with low latency.

10. Implementation Details

10.1. Detailed Network Structure

Figure 10 illustrates the neural network architecture and detailed parameters employed by RENO. The model parameters are shared across all point cloud scales.

10.2. Configuration of Comparative Methods

G-PCCv23⁷ is employed following the Common Test Condition (CTC) recommended by the MPEG committee. For KITTI point clouds, the coordinates are scaled by dividing by 0.001, and the $posQ$ parameter is adjusted to achieve different bitrates. After decoding, the reconstructed point clouds are rescaled to the original coordinate system by multiplying by 0.001. For Ford point clouds, as they are already quantized to 1 mm precision, the original coordinate system is retained.

DracoPy⁸, utilizing Google’s Draco version 1.5.2, is employed for compression in this study. Despite its longevity, Draco remains a benchmark for real-time scenarios [20]. The compression level is maintained at its default setting of 1, while the quantization bits are adjusted to achieve varying compression ratios.

R-PCC⁹ is considered as a baseline for range image-based compression. The BZip2 compressor is employed for

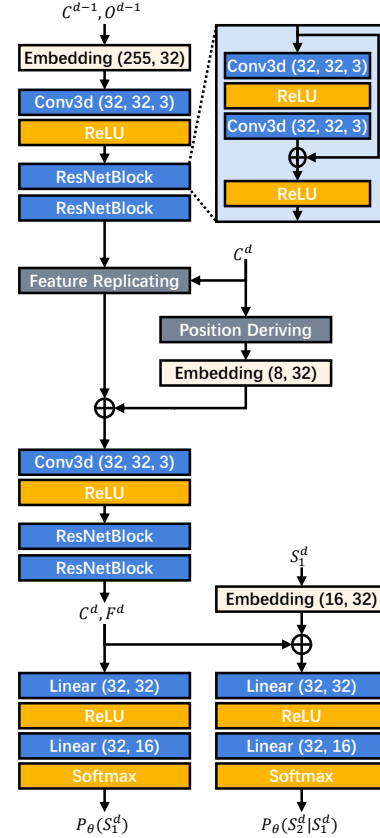


Figure 10. Detailed network structure of the devised Target Occupancy Predictor (TOP). “Conv3d” represents 3D sparse convolution, with parameters defined as (input channels, output channels, kernel size); “Embedding” maps discrete variables according to (dictionary size, vector dimension); “Linear” applies an affine linear transformation with parameters (input channels, output channels); “ \oplus ” denotes element-wise addition.

the optimal compression rate, and varying compression ratios are achieved by adjusting the *accuracy* parameter.

RTST¹⁰ is employed as an additional range image-based compression approach. Single-frame compression mode is adopted, and the horizontal and vertical degree granularities are systematically varied to attain different compression ratios. Note that it is currently supports only the KITTI dataset.

Remark. We observe a notable discrepancy between our experimental results and those reported in the original R-PCC paper [39], which reported markedly superior performance of R-PCC over G-PCC. This divergence primarily stems from methodological differences in PSNR computation. Specifically, the original implementation of R-PCC (as verified through their GitHub repository) employs back-projected geometry rather than original point cloud data

⁷<https://github.com/MPEGGroup/mpeg-pcc-tmc13>

⁸<https://github.com/seung-lab/DracoPy>

⁹<https://github.com/StevenWang30/R-PCC>

¹⁰<https://github.com/horizon-research/Real-Time-Spatio-Temporal-LiDAR-Point-Cloud-Compression>

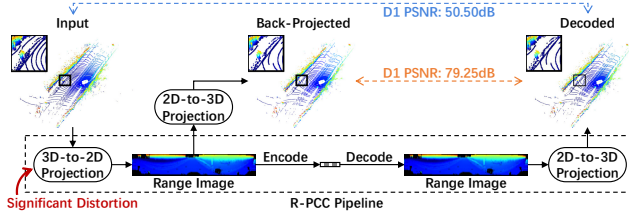


Figure 11. Ours (blue line) vs. R-PCC (orange line) PSNR evaluations. A point cloud from the KITTI dataset is utilized as an exemplar. The setting of PSNR peak value is consistent at 59.70.

as ground truth, thereby circumventing projection-induced distortions illustrated in Fig. 11. The projection distortion is confirmed in both prior studies [42] and our experiments. In contrast, our calculation is more reasonable and aligns with prior arts.

10.3. Metrics

PSNR. The MPEG PCC quality measurement software version 0.13.4 is used to report PSNR values. The peak values are set to 59.70 for KITTI point clouds and 30,000 for Ford point clouds, following conventional practices [11, 16, 31].

Chamfer Distance. The Chamfer Distance in the Fig. 1 of the main manuscript serves as an auxiliary description of point-level distortion. This metric is computed using the following mathematical formulation, implemented according to the Point Cloud Utils¹¹:

$$\begin{aligned} \text{chamfer}(P_1, P_2) = & \frac{1}{2n} \sum_{i=1}^n |x_i - \text{NN}(x_i, P_2)| \\ & + \frac{1}{2m} \sum_{j=1}^m |x_j - \text{NN}(x_j, P_1)| \quad (14) \end{aligned}$$

where $P_1 = \{x_i\}_{i=1}^n$ and $P_2 = \{x_j\}_{j=1}^m$ refer to two point cloud samples; $\text{NN}(x, P) = \text{argmin}_{x' \in P} \|x - x'\|$ is the nearest neighbor function.

11. More Subjective Results

More visualization results are provided in Fig. 12. As seen from the leftmost column ($D=12$), RENO reconstructs point cloud samples with shapes sufficient to distinguish object categories at around 50 ms latency, differing mainly in fine details. For 14-bit precision ($D=14$), it achieves real-time reconstruction with details closely matching the originals.

¹¹https://fwilliams.info/point-cloud-utils/sections/shape_metrics/

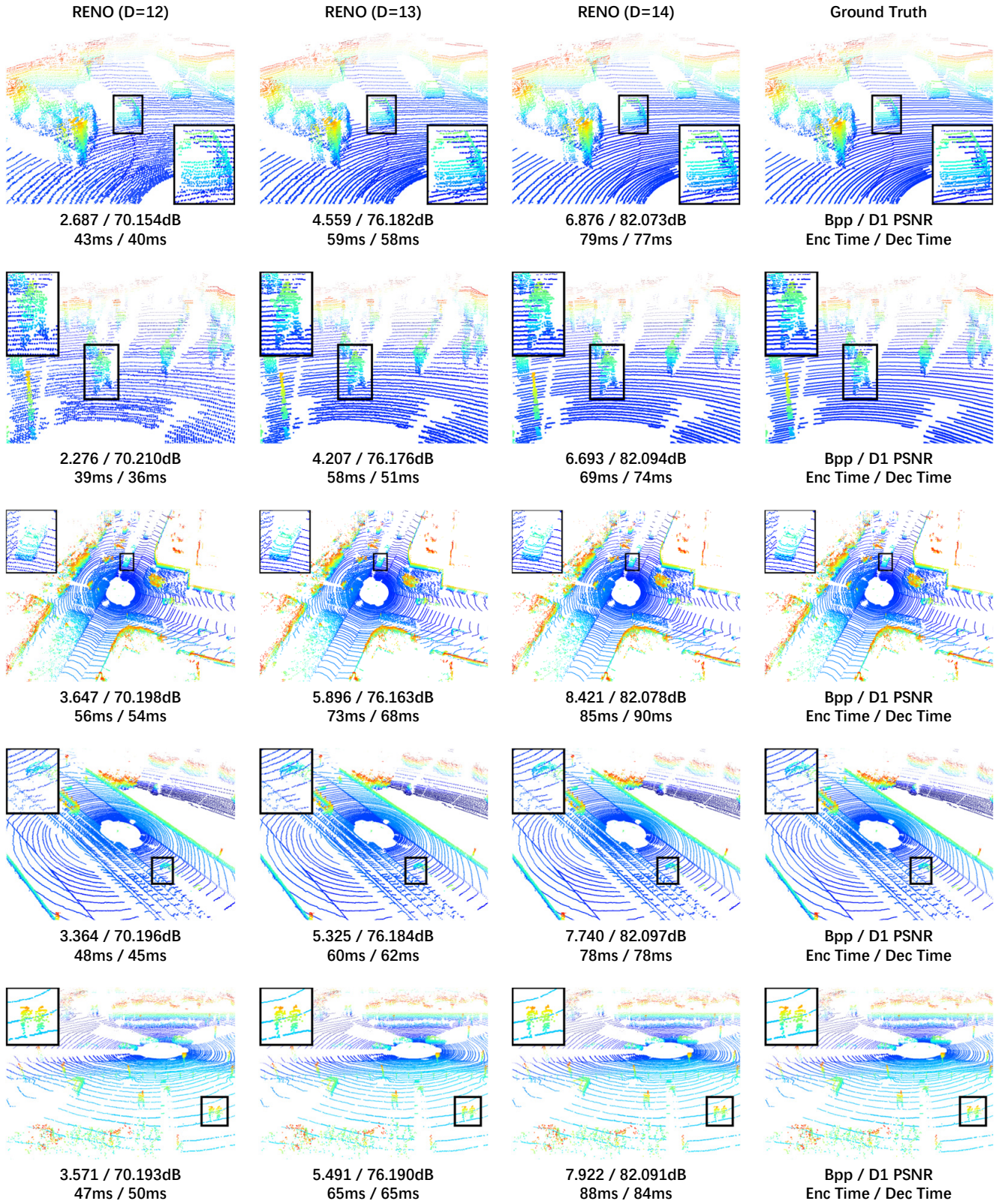


Figure 12. Visualization of compression results for KITTI point cloud. The reconstruction results of RENO under bit depths (D) of 12, 13, and 14 are presented.